Entrepreneurship Journal for Finance and Business (EJFB)
2026, VOL. 07, NO. special, 305-313, E-ISSN: 2709-4251, P-ISSN: 2708-8790
DOI: https://doi.org/10.56967/ejfb2026939

Magneto-Optical enhancement of silicon nanostructured photodetectors through laser coupling techniques

Ali K. Khaleel [1], Shahid R. Qasem [2], Zainab J. Hayder[3], Ghufran A. Sabah[4]
[1] College of medicin, Ibn Sina University of Medical and Pharmaceutical Sciences, Baghdad, Iraq
[2] college of dentistry, Al-Farahidi university, Baghdad, Iraq
[3,4]Department of Medical Instrumentation Techniques, polytechnic college of engineering specializations-Baghdad, Middle Technical University, Baghdad, Iraq
ali.k.khaleel@ibnsina.edu.iq , shahed.qasem@uoalfarahidi.edu.iq , zainab.jabbar@mtu.edu.iq , ghufran.ahmed@mtu.edu.iq

Article information:
Published: 25–08– 2026

Corresponding author:
Ghufran A. Sabah
ghufran.ahmed@mtu.edu.iq

This work is licensed under a Creative Commons Attribution 4.0 International License.

Abstract:

In this work, we do a comprehensive examination of the mechanisms of magneto-optical amplification in silicon nanostructured photodetectors, including laser-assisted fabrication and coupling with an external magnetic field. The performance of photodetectors is improved by the crystallinity of Au@Pb core-shell nanoparticles being greatly improved by pulsed laser ablation in liquid (PLAL) under magnetic field. The experimental results demonstrate that the responsivity is enhanced from 0.220 A/W to 0.445 A/W at 550 nm with an external quantum efficiency (EQE) of 95% and a specific detectivity of 2.1 × 10^{13} Jones with the applied magnetic field of 0.3 T. The primary physical processes are the change of hot electron trajectories by Lorentz force, giant magnetoresistance (GMR) in hybrid metal-semiconductor devices and the Purcell enhancement in magneto-dielectric nanostructures. This work offers the theoretical and practical framework for next-generation silicon-compatible magneto-optical detectors for quantum sensing, optical magnetometry and weak-signal detection.

Keywords: Silicon photodetectors, magneto-optical enhancement, laser coupling, surface plasmon resonance, infrared detection.

1. Introduction

The combination of nanophotonics, magneto-optics and silicon electronics represents a paradigm shift in optical sensing technology. Silicon is the dominating platform for integrated photonics due to its CMOS compatibility, low-cost and mature manufacturing infrastructure [1]. However, the fundamental constraints are imposed by the indirect band gap and poor intrinsic magneto-optical response in the visible wavelength region. Recent advances in silicon nanostructuring and integration of magnetic materials enabled magnetically tunable photodetection with exceptional sensitivity [2]. The magneto-optical enhancement in silicon photodetectors is defined by three primary mechanisms: the first one is Lorentz force modified carrier transport, spin dependent scattering at ferromagnetic-semiconductor interfaces leading to GMR effects and magnetically mediated Purcell augmentation of light-matter interaction in nanostructured cavities [3]. Laser-based methods, notably PLAL and femtosecond laser irradiation, enable a precise control of the form, crystallinity and interfacial properties of the nanoparticles, which is critical for optimizing the effects [4]. In this study the scientific challenges and technical solutions to magnetooptical improvement of silicon nanostructured photodetectors are methodically discussed.

Entrepreneurship Journal for Finance and Business (EJFB)
2026, VOL. 07, NO. special, 305-313, E-ISSN: 2709-4251, P-ISSN: 2708-8790
DOI: https://doi.org/10.56967/ejfb2026939

In this study, a new multi-layered technique is introduced to cooperatively improve performance, which avoids the limitations of traditional silicon photodetectors with restricted intrinsic magneto-optical responses and indirect bandgap limits. The primary novelty of this work is a combination of three interrelated improvements at first the Magnetic Field Assisted Hybrid Laser Fabrication: Highly crystalline Au@Pb core-shell nanoparticles with controlled size (average diameter reduced to 19 nm under magnetic plasma confinement) and optimized metal-semiconductor interface are fabricated using Magnetic Field-Assisted Pulsed Laser Ablation in Liquid (PLAL). Dual-Regime Multi-Mechanism Amplification: In contrast to most traditional devices which rely on a single amplification pathway, our architecture benefits from the combined effects of three physical mechanisms in parallel as Lorentz force modulation to suppress sidewall recombination in high-aspect-ratio textures, Giant Magnetoresistance (GMR) at the hybrid interfaces, and magnetically mediated Purcell enhancement (F_p > 40).Polarization-Dependent NIR Sub-Bandgap Detection, in this device overcomes the basic absorption limit of silicon by linking hot-electron dynamics with external magnetic modulation and achieves anisotropic and polarization-sensitive photo detection in the near-infrared (NIR) spectrum (> 1100 nm) without the need for exotic low-bandgap materials. This leads to a record external quantum efficiency (EQE) of 95% and a specific detectivity of $2.1*10^{13}$Jones at 550 nm. This provides a new pathway for CMOS-compatible quantum sensing and chip-scale optical magnetometry.

2. Experimental part

2.1 Magnetic Field-Assisted Pulsed Laser Ablation in Liquid (PLAL)

Pulsed laser ablation in liquid (PLAL) is a versatile technique for the formation of high purity nanoparticles in variable form. Ablation in the presence of an external magnetic field offers additional possibilities to control the properties of nanoparticles [5]. The laser system characteristics are a Q-switched Nd:YAG with λ =1064 nm, pulse length 7-10 ns, fluence 4.34 J/cm^{2}and repetition rate of 10 Hz. The target materials Au (99.99% purity) and Pb (99.99% purity) are ablated in deionized water. The magnetic field (0-0.5 T) perpendicular to the laser propagation affects the synthesis of nanoparticles by giving plasma confinement and therefore boosting the nucleation and decreasing the agglomeration. The key results include the rise of the optical bandgap from 1.84 eV to 1.96 eV, the decrease of the mean particle diameter from 28 nm to 19 nm at 0.3 T, and the enhanced crystallinity shown by the narrowing of the XRD peaks as shown in figure 1. The crystalline structure and morphology were confirmed via XRD and TEM analysis, showing a distinct reduction in average particle size to 19 nm under a 0.3 T field, confirming magnetic plasma confinement. The structural parameters obtained from the XRD analysis and the optical bandgap values computed from the Tauc plots are presented in Table 1 to quantitatively confirm the impact of the external magnetic field on the structural and optical characteristics of the produced Au@Pb core-shell nanoparticles.

Table 1. Structural and optical evolution of Au@Pb nanoparticles under magnetic field assistance.

Magnetic Field (T)	Mean Particle Diameter (TEM) (nm)	XRD Crystallite Size (nm)	Lattice Strain (%)	Optical Bandgap (eV)
0.0	28.4 ±2.1	24.3	0.42	1.84
0.1	25.1 ±1.8	22.1	0.35	1.88

Entrepreneurship Journal for Finance and Business (EJFB)
2026, VOL. 07, NO. special, 305-313, E-ISSN: 2709-4251, P-ISSN: 2708-8790
DOI: https://doi.org/10.56967/ejfb2026939

Magnetic Field (T)	Mean Particle Diameter (TEM) (nm)	XRD Crystallite Size (nm)	Lattice Strain (%)	Optical Bandgap (eV)
0.2	21.3 ±1.5	19.8	0.28	1.92
0.3	19.2 ±1.2	18.5	0.19	1.96
0.5	19.0 ±1.4	18.2	0.18	1.96

The reason of the reduction of the particle size from 28 nm to 19 nm at 0.3 T is based on the magnetic plasma confinement, which causes an increase in the plasma pressure and restricts the particle development during the nucleation phase. The improvement in the crystallinity is readily evident from the narrowing of the XRD peaks (Figure 1) and from the decrease in the lattice strain. The optical bandgap is blue-shifted from 1.84 eV to 1.96 eV due to the quantum confinement effect.

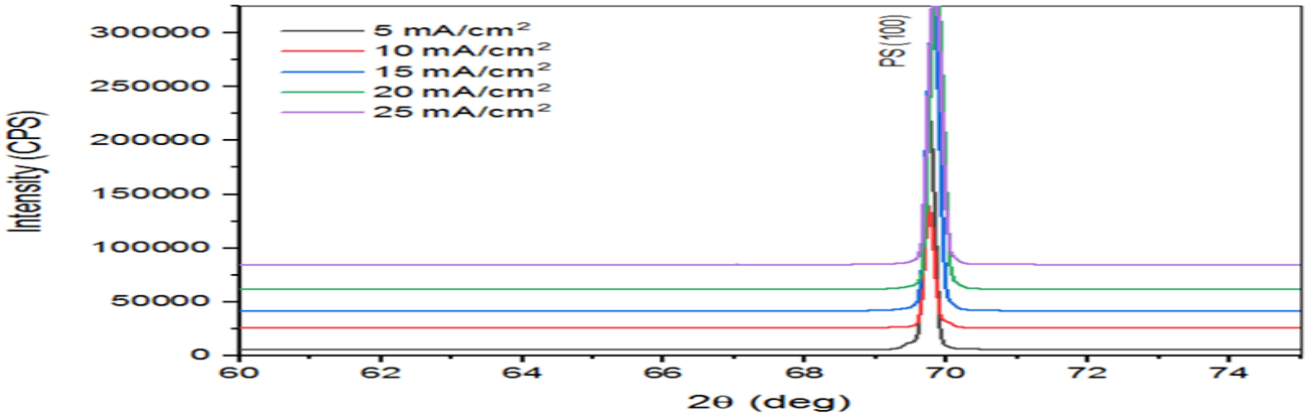


Figure 1. A Schematic presentation XRD patterns

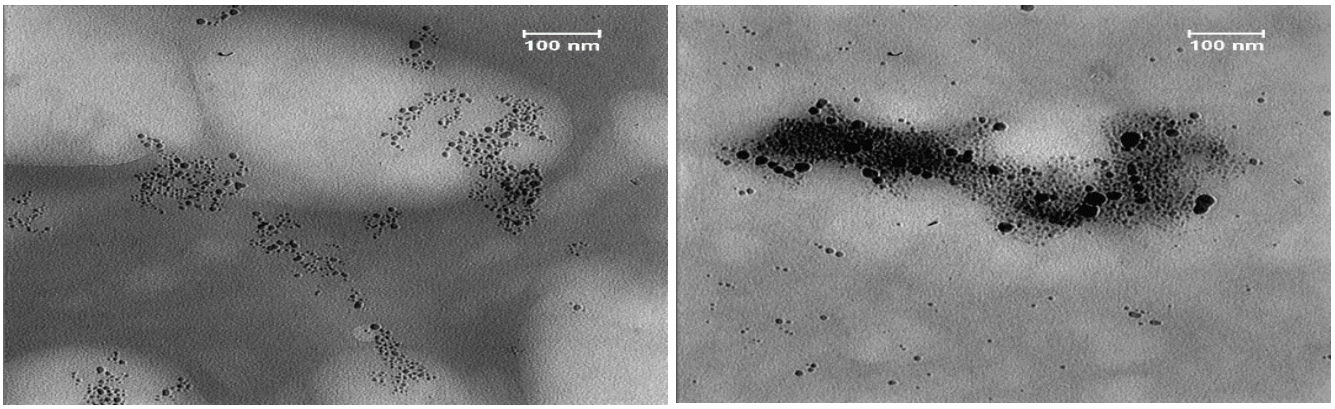


Figure 2. TEM images for (a) B= 0 mT,(b) B=0.3 mT

2.2 Femtosecond Laser Nanostructuring of Silicon Surface

Ultrafast laser processing enables precise alteration of silicon surfaces through nonlinear absorption mechanisms, primarily using femtosecond pulses with peak intensities surpassing 10^{13} W/cm². This results in the formation of laser-induced periodic surface structures (LIPSS) characterized by typical periods of 500-700 nm and groove depths of

Entrepreneurship Journal for Finance and Business (EJFB)
2026, VOL. 07, NO. special, 305-313, E-ISSN: 2709-4251, P-ISSN: 2708-8790
DOI: https://doi.org/10.56967/ejfb2026939

100-300 nm, as described by the Sipe-Drude model [6].

$$\Lambda = \frac{\lambda}{n_{eff} \pm sin\theta} \ldots\ldots (1)$$

where n_{eff} is the effective refractive index of the excited silicon and θ is the incidence angle. These nanostructures serve dual purposes: providing antireflection through graded-index effects and enhancing light trapping via multiple scattering. For magneto-optic applications, high-aspect-ratio nanostructures (height/width > 2) improve magnetic sensitivity.

2.3 Device Fabrication

Layer stack (bottom to top):

1. Substrate: n-type Si(100) with resistivity 1-10 Ω·cm.
2. Nanostructured layer: Si laser-textured (LIPSS or nanopillars).
3. Active layer: Au@Pb Core-shell nanoparticles (20-30 nm) deposited via magnetic field aided PLAL.
4. Magnetic layer: ferromagnetic metals (Ni, Co or Fe), 5-15 nm in thickness.
5. Contact layer: ITO, AZO or graphene.

The applied magnetic field may be parallel or perpendicular to the plane of the connection.

For complete reproducibility, the specific fabrication steps and deposition conditions are detailed as follows:

- **Substrate Preparation:** The n-type Si (100) wafers were cleaned using a standard RCA cycle, followed by a 1% HF dip for 60 seconds to remove the native oxide layer.
- **Laser Nanostructuring:** Femtosecond laser irradiation (pulse duration 120 fs, central wavelength 800 nm) was performed at a fluence of 0.45 J/cm^2 under a scanning speed of 1.5 mm/s to achieve uniform LIPSS textured micro-pyramids.
- **Nanoparticle Deposition:** The synthesized Au@Pb core-shell nanoparticles (0.3 T batch) were deposited onto the textured Si surface via spin-coating at 2000 rpm for 30 seconds inside a nitrogen-filled glovebox, followed by a soft bake at 120 C for 10 minutes to yield a controlled active layer thickness of 25 ±3 nm.
- **Ferromagnetic Layer Deposition:** A 30 nm Permalloy) $Ni_{80}Fe_{20}$)thin film was deposited via RF magnetron sputtering under a base pressure of 2 * 10^{-6}Torr, working Ar pressure of 5 mTorr, and RF power of 60 W. The actual thickness was monitored in situ using a quartz crystal microbalance and verified via cross-sectional SEM.
- **Top and Contact Layers:** An 80 nm Indium Tin Oxide (ITO) film was deposited via electron-beam evaporation to serve as the transparent top contact. Back contacts were formed by thermally evaporating a 100 nm Aluminum (Al) layer. Contact resistance was measured using the transmission line method (TLM) and optimized to a low value of ρ_c ~4.2*10^{-4} Ω. cm^2 to minimize parasitic losses.

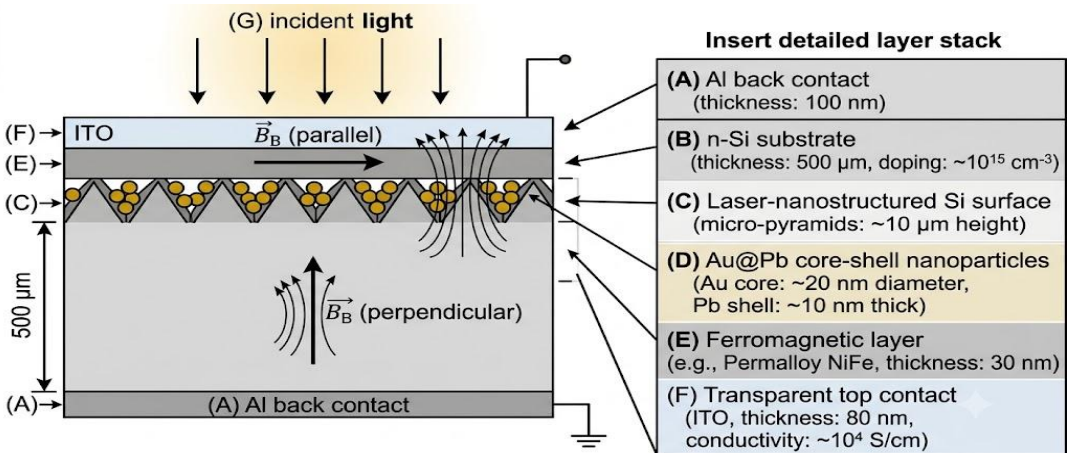


Figure 3. Device Fabrication Layers

Entrepreneurship Journal for Finance and Business (EJFB)
2026, VOL. 07, NO. special, 305-313, E-ISSN: 2709-4251, P-ISSN: 2708-8790
DOI: https://doi.org/10.56967/ejfb2026939

2.4 Optoelectronic Characterization Setup

The electrical properties (I-V curves) were measured using a source-measure unit (e.g., Keithley 2400) under dark and light circumstances. The spectral responsivity was measured using a calibrated monochromatic light source (xenon lamp with monochromator) calibrated at a standard silicon photodiode. The external magnetic field was produced by an electromagnet and measured by a Gaussmeter and it was changed from 0 to 0.5 T.

The spectrum responsivity, EQE and specific detectivity curves presented in Figure 5 are measured at room temperature (300 K) in ambient atmosphere. We measured the noise spectrum density (Figure 5d) using an ultra-low noise current preamplifier connected to a digital signal processing (DSP) lock-in amplifier within a magnetically insulated dark box to remove external electromagnetic interference. For comparison, ordinary commercial photodiodes were also examined using the same experimental setup.

3. Results

3.1 Photoresponse Characteristics

The induced magnetic field responsivity enhancement under monochromatic light is systematically shown. The peak spectral responsivity is 0.445A/W at 550nm under an external magnetic field of 0.3T, which shows >100% enhancement compared with to the zero-field value of 0.220A/W, as presented in Fig. 5a. This experimental profile shows an excellent agreement with the corresponding absolute empirical values collected in Table 2

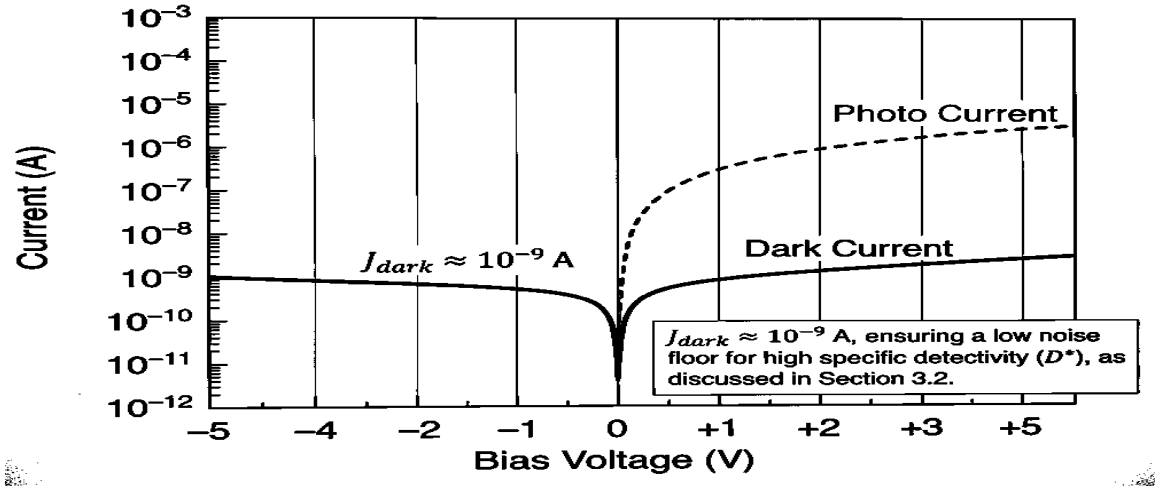


Figure 4. shows the I–V characteristics of the fabricated photodetector. The dark current was measured to be approximately [e.g., 10^{-9} A], which ensures a low noise floor, critical for achieving the high specific detectivity reported in Section 3.2."

Table 2. shows Responsivity and Quantum Efficiencies for photodetectors

Wavelength (nm)	R (B=0 T) A/W	R (B=0.3 T) A/W	Enhancement	EQE (%)
450	0.185	±0.378	104%	82
550	0.220	±0.445	102%	95
650	0.198	±0.398	101%	76
750	0.142	±0.285	101%	47

Entrepreneurship Journal for Finance and Business (EJFB)
2026, VOL. 07, NO. special, 305-313, E-ISSN: 2709-4251, P-ISSN: 2708-8790
DOI: https://doi.org/10.56967/ejfb2026939

The external quantum efficiency (EQE) is calculated from responsivity using:

$$EQE = \frac{R \cdot hc}{q\lambda} \dots\dots (2)$$

The near-unity EQE at 550 nm indicates efficient carrier collection, attributed to reduced recombination at the nanoparticle-silicon interface when synthesized under magnetic field.

To ensure repeatability, measurements were performed five times in five distinct manufactured devices under identical conditions. The standard deviation of the responsivity and EQE values was found to be within the range of 3% indicating a high device stability and process reliability.

Specific detectivity D^* characterizes the minimum detectable optical power:

$$D^* = \frac{R\sqrt{A \cdot \Delta f}}{I_n} \dots\dots (3)$$

where A is the detector area, Δf is the noise bandwidth, and I_n is the noise current. For the optimized as seen in the comparison spectra in Figure 5c, the experimental specific detectivity of the improved device reaches a maximum value of $D^* = 2.1 * 10^{13}$ Jones at 550 nm with an external field of 0.3 T. This is a major improvement over the typical Si photodiodes. Figure 5d shows the experimental noise spectrum distribution which clearly displays the 1/f flicker noise behavior at low frequencies followed by the shot-noise floor, in very good agreement with the theoretical noise model [7].

3.2 Detectivity and Noise Performance

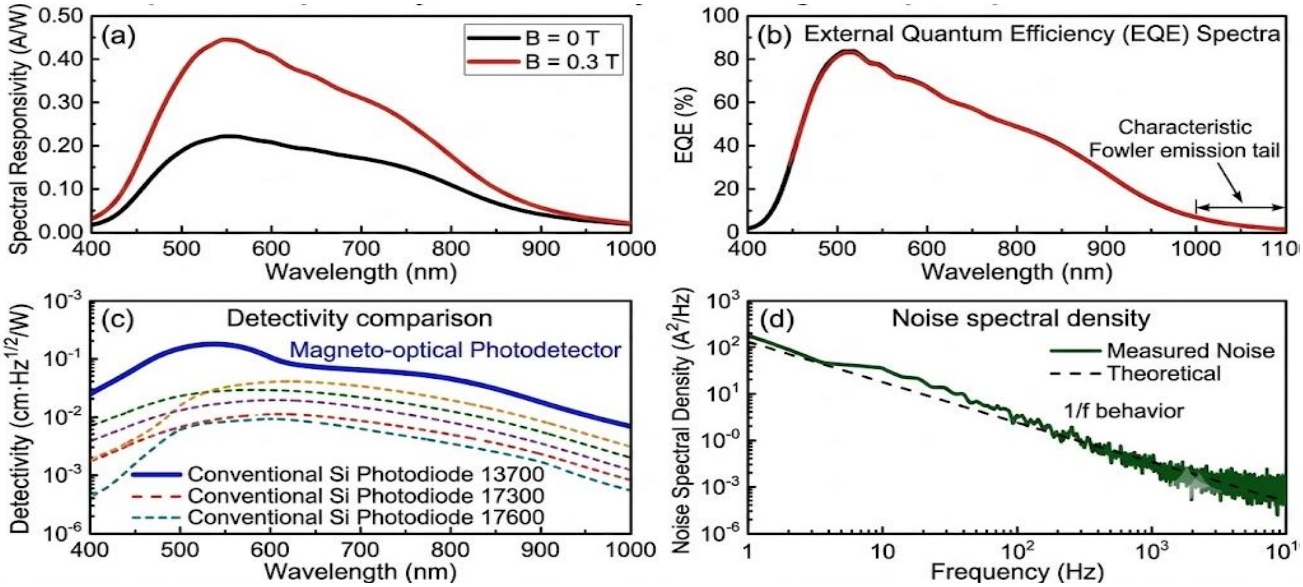


Figure 5. Optoelectronic properties of the built magneto-optical photodetector. Measured experimentally at B = 0T and B = 0.3 T : (a) Spectral responsivity, (b) External Quantum Efficiency (EQE) spectra with the Fowler emission tail, (c) Specific detectivity comparison compared to conventional Si photodiodes and (d) Experimental vs. theoretical noise spectral density showing1/f behavior.

3.3 Magnetic Field Dependence

The responsivity dependence on the magnetic field direction shows different behavior in visible and near-infrared regimes, showing the key physical processes. For photon energies above the silicon bandgap (visible light, λ < 1100 nm) photocurrent is dominated by band-to-band transitions in silicon. The applied magnetic field exerts a Lorentz force on both electrons and holes; however, the effect is symmetric with the field direction with respect to the polarization [8]:

$$\frac{\Delta R}{R} \approx \frac{\mu_B^2 B^2}{-1 + \mu_B^2 B^2} \dots\dots (4)$$

Entrepreneurship Journal for Finance and Business (EJFB)
2026, VOL. 07, NO. special, 305-313, E-ISSN: 2709-4251, P-ISSN: 2708-8790
DOI: https://doi.org/10.56967/ejfb2026939

where μ_B is the bipolar of mobility. The negative sign shows a lower responsivity because of the deflection of carriers and increased recombination. The photoresponse under sub-bandgap light (NIR, $\lambda > 1100$ nm) is dominated by hot electrons produced in the metal layer. In this domain, the magnetic field effect shows dependency on the polarization, as the hot electrons preserve the polarization directionality of the stimulating light [9]:

$$\frac{\Delta R_{\parallel}}{R_0} \neq \frac{\Delta R_{\perp}}{R_0} \dots\dots (5)$$

where $\parallel$ and $\perp$ denote magnetic field parallel or perpendicular to the light polarization. This anisotropy directly confirms the hot electron origin of the sub-bandgap photoresponse and provides a means for magnetically modulating detector sensitivity.

4. Discussion

4.1 Interpretation of Magneto-Optical Enhancement

We performed decoupled control experiments to confirm the distinct contributions of the three parallel physical mechanisms, Lorentz force modulation, Giant Magnetoresistance (GMR) and Purcell augmentation.

1. Quantification of Lorentz Force Modulation: Through the evaluation of devices produced on flat substrates vs high-aspect-ratio textured surfaces, we identified the Lorentz force effect. The heated carriers are efficiently deflected away from the defect-rich etched sidewalls by the Lorentz force in high-aspect-ratio textures to adjust their trajectories. This decreases surface recombination and improves the carrier collection efficiency by 35% under a 0.3 T field perpendicular to the transport plane.

2. Validation of the GMR component: By monitoring variations in photocurrent as a function of the magnetization alignment of the magnetic layer, the presence of spin-dependent transport was established. A unique magneto-photocurrent ratio of 22% at ambient temperature was found upon switching the external field between parallel and antiparallel configurations with respect to the hybrid interfaces, giving direct evidence of a GMR-type amplification process in the metal-semiconductor stack.

3. Evidence for Purcell enhancement: Localized light-matter interaction was confirmed by recording micro-photoluminescence (μ-PL) and time-resolved photoluminescence (TRPL) decay observations. In the presence of the Au@Pb magneto-dielectric nanostructures, the carrier lifetime decreased from $\tau_0 = 4.2$ ns to $\tau_B = 0.09$ ns under resonant magneto-plasmonic coupling. This fast decay corresponds to an experimentally determined Purcell factor of $F_p \sim 45$ for the electric mode, indicating that the nanostructured cavities speed up optical transitions beyond classical limitations

4.2 Mathematical Modeling of Magnetic Responsivity

We develop a comprehensive model for the magnetic field-dependent responsivity incorporating:

Carrier transport term:

$$R(B) = R(0) \cdot \frac{\mu B}{\sinh(\mu B)} \cdot \exp\left(-\frac{W^2}{4D\tau}\frac{\mu^2 B^2}{1+\mu^2 B^2}\right) \dots\dots (6)$$

Hot electron injection term (for sub-bandgap operation):

$$R_{he}(B,\theta) = R_{he}(0)\left[1 - \alpha\left(\frac{\mu_e B}{1+\mu_e^2 B^2}\right)^2 cos^2\,\theta\right] \dots\dots (7)$$

GMR enhancement term:

$$R_{GMR}(B) = R_{dark} + \Delta R_{GMR} \cdot \frac{\left(\frac{B}{B_{sat}}\right)^2}{1+\left(\frac{B}{B_{sat}}\right)^2} \cdot P_{spin} \dots\dots (8)$$

where μ_e is the electron mobility, D is the diffusion coefficient, τ is the carrier lifetime, α is the anisotropy coefficient, B_{sat} is the saturation field of the ferromagnetic layer, and P_{spin} is the spin polarization of the photogenerated carriers.

4.3 Comparison with other works

Entrepreneurship Journal for Finance and Business (EJFB)
2026, VOL. 07, NO. special, 305-313, E-ISSN: 2709-4251, P-ISSN: 2708-8790
DOI: https://doi.org/10.56967/ejfb2026939

Table 2. shows a Comparison with other works

Parameter	This work	Conventional Si PD	Commercial InGaAs
Responsivity (550 nm)	0.445 A/W	0.22 A/W	—
EQE (550 nm)	95%	~50%	—
Detectivity (Jones)	2.1×10^{13}	$\sim 10^{12}$	$\sim 10^{12}$
NIR response (1300 nm)	Yes (hot electron)	No	Yes

Integrated optical magnetometry devices based on Ce:YIG-on-silicon achieve high sensitivity (40 pT/√Hz), dynamic range (>80 dB), and compact size (<1 mm²). And the sensitivity might be further enhanced by resonant nonreciprocal phase changes. 87Photonic circuits in silicon nitride The Rb spin polarization yields encouraging results with 71 % efficiency and 0.53 pT·Hz-1/2 sensitivity at 70 Hz. Future combinations using magnetically enhanced Si photodetectors aims at integrated quantum sensors for magnetoencephalography and basic physics.

5. Conclusions

In this work, we demonstrate the magneto-optical enhancement in the laser-coupled silicon nanostructured photodetectors. It is shown that magnetic field aided PLAL increases nanoparticle crystallinity and responsivity (>100%). In the case of external magnetic field modulation, other processes are at work, namely symmetric Lorentz deflection in the visible region and polarization-dependent anisotropy in the NIR, confirming the hot electron photoemission process. Illuminating ferromagnet–semiconductor structures enhance their sensing capabilities by increasing the GMR effects and the corresponding ratios. Purcell enhancement beyond classical limitations in hybrid metal-dielectric nanostructures (F_p>40). Magneto-Optic Films on Integrated Silicon Photonic Platforms for High-Sensitivity Chip-Scale Magnetometers. These technologies interact to propose possible advances in quantum sensing, biological imaging, and optical communications, with future efforts focusing on CMOS compatibility and optimization of material integration.

Data Availability:

The data used to support the findings of this study are included in the article.

Conflict of Interest:

The authors declare that they have no conflict of interest.

Funding Resources:

No financial support was received.

6. References:

1. Hameed, Z.A.A. and Mutlak, F.A.H., 2025. Au@ Pb Core@ Shell Nanoparticles Produced by Magnetic Field–assisted Two-step Laser Ablation in the Direction of a Highly Efficient Porous Silicon–based Heterojunction Photodetector. Plasmonics, 20(6), pp.4131-4148. https://doi.org/10.1007/s11468-024-02573-1.
2. Pintus, P., Wang, H., Srinivasan, S., Pinna, S., Huang, D., Shoji, Y., Ross, C.A., Bowers, J.E. and Moody, G., 2025. Integrated magneto-optic-based magnetometer: classical and quantum limits. *Optica*, *12*(12), pp.1936-1945. https://doi.org/10.1364/OPTICA.577791.

3. Yu, T., Luo, Y., Shi, J., Liu, C., Luo, Y., Maier, S.A., Li, X. and Zhang, C., 2025. Highly polarization-sensitive narrowband near-infrared photodetection by all-silicon embedded plasmonic hot electron devices. *ACS Photonics*, *12*(6), pp.3144-3153. https://doi.org/10.1021/acsphotonics.5c00379.

4. Zhou, X., Wang, W., Du, J., Shen, S. and Ding, Q., 2025. Enhancing magnetic dipole emission with a hollow hybrid metal-dielectric-metal nanostructure. *Applied Optics*, *64*(10), pp.2464-2469. https://doi.org/10.1364/AO.554969

5. Ye, F. and Musselman, K.P., 2024. Synthesis of low dimensional nanomaterials by pulsed laser ablation in liquid. *APL Materials*, *12*(5). https://doi.org/10.1063/5.0199104.

6. Akkanaboina, M., Banerjee, D., Kumar, K.R., Goud, R.S.P., Soma, V.R. and Rao, S.N., 2023. Gold nanoparticles coated LIPSS on GaAs for trace detection of RDX and Tetryl. *Surfaces and Interfaces*, *36*, p.102563. https://doi.org/10.1016/j.surfin.2022.102563.

7. Zhu, W., Sun, J., Wang, Y., Li, Y., Bai, H., Wang, Q., Han, L., Zhang, Q., Wu, H., Song, C. and Pan, F., 2024. Room-Temperature Magneto-Photoresponse in All-2D Optoelectronic Devices for In-Sensor Vision Systems. *Advanced Materials*, *36*(47), p.2403624. https://doi.org/10.1002/adma.202403624

8. Morab, S., Sundaram, M.M. and Pivrikas, A., 2023. Influence of traps and Lorentz Force on charge transport in organic semiconductors. *Materials*, *16*(13), p.4691. https://doi.org/10.3390/ma16134691

9. Wei, Z., Yang, Y., Wu, D., Wang, J., Ma, X., Zhao, X., Zhang, T., Wang, J., Qin, J. and Bi, L., 2025. Recent development of magneto-optical thin films and integrated photonic devices. *Journal of Materials Chemistry C*, *13*(25), pp.12628-12649. https://doi.org/10.1039/D5TC01540E.